



Room-Temperature Ferroelectricity in 1T'-ReS₂ Multilayers

Yi Wan,^{1,3,§} Ting Hu,^{1,§} Xiaoyu Mao,^{2,§} Jun Fu,² Kai Yuan,^{3,4} Yu Song,⁵ Xuetao Gan,⁵ Xiaolong Xu,³
Mingzhu Xue,³ Xing Cheng,³ Chengxi Huang,¹ Jinbo Yang^{1,3,4} , Lun Dai,^{3,4,*}

Hualing Zeng^{1,2,†} and Erjun Kan^{1,‡} 

¹MIT Key Laboratory of Semiconductor Microstructure and Quantum Sensing, and Department of Applied Physics, Nanjing University of Science and Technology, Nanjing 210094, China

²International Center for Quantum Design of Functional Materials (ICQD), Hefei National Laboratory for Physical Sciences at the Microscale, and Department of Physics, University of Science and Technology of China, Hefei 230026, China

³State Key Laboratory for Artificial Microstructure & Mesoscopic Physics, School of Physics, Peking University, Beijing 100871, China

⁴Collaborative Innovation Center of Quantum Matter, Beijing 100871, China

⁵MOE Key Laboratory of Material Physics and Chemistry under Extraordinary Conditions, and Shaanxi Key Laboratory of Optical Information Technology, School of Science, Northwestern Polytechnical University, Xi'an 710072, China



(Received 16 May 2021; accepted 23 December 2021; published 8 February 2022)

van der Waals materials possess an innate layer degree of freedom and thus are excellent candidates for exploring emergent two-dimensional ferroelectricity induced by interlayer translation. However, despite being theoretically predicted, experimental realization of this type of ferroelectricity is scarce at the current stage. Here, we demonstrate robust sliding ferroelectricity in semiconducting 1T'-ReS₂ multilayers via a combined study of theory and experiment. Room-temperature vertical ferroelectricity is observed in two-dimensional 1T'-ReS₂ with layer number $N \geq 2$. The electric polarization stems from the uncompensated charge transfer between layers and can be switched by interlayer sliding. For bilayer 1T'-ReS₂, the ferroelectric transition temperature is estimated to be ~ 405 K from the second harmonic generation measurements. Our results highlight the importance of interlayer engineering in the realization of atomic-scale ferroelectricity.

DOI: [10.1103/PhysRevLett.128.067601](https://doi.org/10.1103/PhysRevLett.128.067601)

The demand for device miniaturization in modern electronics stimulates the exploration of two-dimensional (2D) ferroelectricity [1,2] in the quantum realm with significant advances in ultrathin van der Waals (vdW) materials recently [3–11]. In these 2D ferroelectrics, spontaneous electric polarization originates from the subtle atomic position displacement from the inversion center within the monolayer, and is strictly constrained by lattice symmetry and structure stability. As a result, only a few vdW crystals have been experimentally verified with intrinsic ferroelectricity until the present [12–28]. To expand the family of 2D ferroelectrics, the layer degree of freedom in vdW materials [29] was utilized to generate so-called sliding ferroelectricity in multilayers via interlayer translation [30–33]. This type of vertical ferroelectricity is, in principle, valid for a wide range of vdW materials; even their monolayer form is centrosymmetric [30–36]. With interlayer engineering, sliding-induced 2D ferroelectricity has been demonstrated in topological semimetal WTe₂ [31–33], metallic twisted bilayer graphene [34,37–39], and insulating AB stacked bilayer hBN [35,36]. These pioneering progresses lead to the emergence of a research field called slidetronics [35,36].

To advance slidetronics, semiconducting vdW materials with a moderate band gap are preferred. The semiconducting nature endows a given material with broader application prospects [2,40], such as the direct integration into optoelectronics and the efficient gate tunability. As a contrast, it is hard to realize these application potentials in a metallic or insulating material system. For example, the spontaneous vertical polarization in multilayer WTe₂ might be screened by the itinerant carriers due to its metallic character, which in turn degrades the importance in practical applications. In this sense, seeking sliding ferroelectricity in vdW semiconductors not only helps to understand the physical origin, but also benefits the potential technical applications.

In this work, we report room-temperature sliding ferroelectricity in semiconducting 1T'-ReS₂ [41–45] multilayers. Using first-principles density function theory (DFT) calculations, we reveal that the electric polarization and interlayer translation are strongly coupled in ReS₂ multilayers, which enables 2D vertical ferroelectricity by interlayer sliding. Nevertheless, monolayer 1T'-ReS₂ is nonferroelectric due to the symmetry forbiddance. Using piezoresponse force microscopy (PFM) and second harmonic generation (SHG), we observe robust vertical

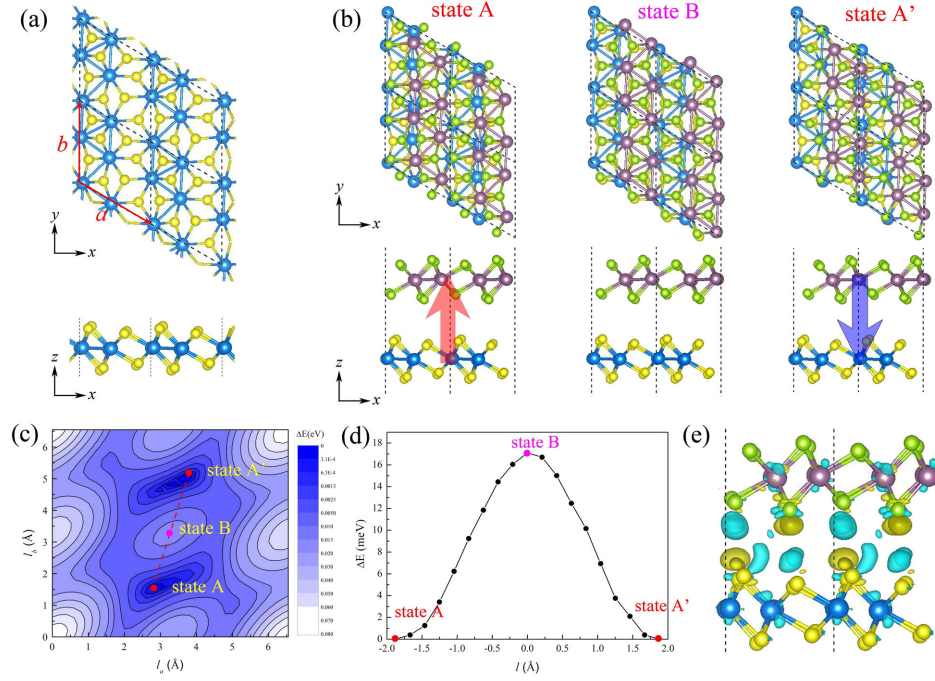


FIG. 1. (a) Top and side views for the crystal structures of monolayer ReS_2 . (b) Top and side views of the two energy-degenerate ferroelectric structures of bilayer ReS_2 (states A and A') and the high-symmetry nonpolar structure (state B). The arrows indicate the polarization direction. (c) The energy contour plot of bilayer ReS_2 versus the sliding distance (l_a, l_b). The contour colors illustrate the total energy of the unit cell relative to the energy of ferroelectric states (red dots). (d) The energy pathway of ferroelectric transition. (e) The charge density difference of bilayer ReS_2 in state A. The yellow and blue colors represent the positive and negative values, respectively.

ferroelectricity in $1\text{T}'\text{-ReS}_2$ with layer number $N \geq 2$ as verified by solid evidences, including the hysteretic switching of polarization, the artificial domain engineering, the clear existence of domain walls, and the measurement of ferroelectric transition temperature. Furthermore, with the 2D vertical ferroelectricity in few-layer $1\text{T}'\text{-ReS}_2$, a ferroelectric tunnel junction (FTJ) device is demonstrated.

Theoretical analysis of the ferroelectric properties in 2D $1\text{T}'\text{-ReS}_2$.—Our first-principles DFT calculations were conducted by the Vienna *ab initio* simulation package (VASP) [46,47], which includes the projected augmented wave method [48] and the Perdew-Burke-Ernzerhof [49] exchange-correlation potential function. As shown in Fig. 1(a), the crystal structure of monolayer ReS_2 contains four formula units in a unit cell. Each Re in monolayer ReS_2 has six neighboring S sites, and the Re atoms are sandwiched by the S atoms at both sides. Because of the Peierl's distortion, monolayer ReS_2 prefers a distorted $1\text{T}'$ structure ($1\text{T}'$) with four adjacent Re atoms bonding together to form diamond-shaped Re chains that extend along the in-plane b axis. The calculated lattice constants are 6.41 and 6.54 Å for the a and b axes, respectively. The a and b axes are with an angle of 119.3° . Because the monolayer ReS_2 belongs to the C_i space group, its inversion symmetry prohibits the emergence of polarization.

For bilayer ReS_2 [Fig. 1(b)], starting from the AA stacking structure with xy -plane mirror symmetry, we slide

the upper layer along the a and b axes by a sliding distance of (l_a, l_b). The energy contour is presented in Fig. 1(c). There are two degenerate minimum points on the energy surface with sliding distance of (2.8 Å, 1.6 Å) and (3.8 Å, 5.2 Å), which are marked as states A and A' [Fig. 1(b)], respectively. They are connected through a saddle point marked as state B with sliding distance of (3.3 Å, 3.4 Å). Compared with states A and A', state B has higher symmetry with a glide plane in the xy plane, which prevents the emergence of vertical polarization. The structures of states A and A' can be obtained from state B by moving the upper layer with a sliding distance of (−0.5 Å, −1.8 Å) and (0.5 Å, 1.8 Å), respectively. The nonequivalence of the top and bottom layers in state A leads to an uncompensated charge transfer between them and results in the vertical polarization. Furthermore, state A' can be obtained via mirror operation on state A with respect to the horizontal plane in the center (see details in the Supplemental Material, S1 [50]). This behavior gives rise to a reversed vertical polarization and therefore hints at the existence of ferroelectricity.

Our Berry-phase calculation based on DFT confirmed the above symmetry analysis. The two degenerate structures (states A and A') have spontaneous vertical polarization with opposite polarization directions, while state B is nonpolar along the z -axis direction. The results indicate that the vertical ferroelectricity is closely related to

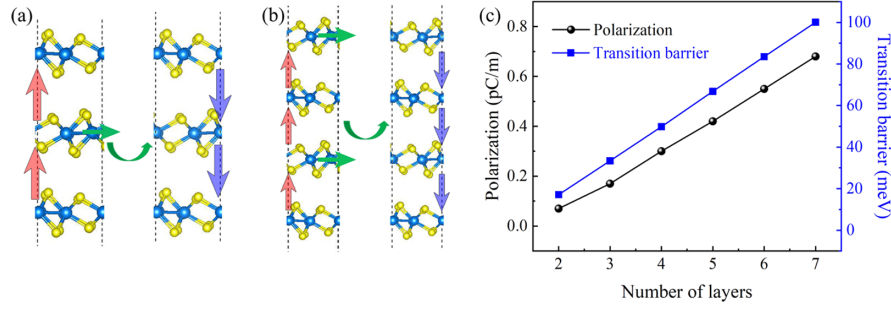


FIG. 2. (a),(b) Ferroelectric switching of ReS_2 in its trilayer (a) and tetralayer (b) form. (c) Layer dependence of polarization values and transition barriers.

interlayer translation, so that it can be switched upon interlayer sliding. The spontaneous polarization at zero temperature is calculated to be 0.07 pC/m. The energy difference between the ferroelectric and the nonpolar states gives an estimation of the transition barrier of ~ 17.1 meV, as shown in Fig. 1(d). To further clarify the origin of the vertical polarization, we calculated the charge density difference between the top and bottom layers in state A. As shown in Fig. 1(e), we find the accumulation and depletion of electrons in the interspace between two individual ReS_2 monolayers. The nonequivalence of the two layers causes a net charge transfer of $0.0003e$ from the top layer to the bottom layer, resulting in the 2D vertical polarization.

A similar mechanism can be applied to ReS_2 multilayers. As shown in Fig. 2(a), the polarization of trilayer ReS_2 can be switched from upward to downward when the middle layer is displaced by (1.0 Å, 3.6 Å). And for the ReS_2 tetralayer [Fig. 2(b)], the polarization is switched if the

second and fourth layers slide by (1.0 Å, 3.6 Å) simultaneously. The layer dependence of the polarization value and the transition barrier are plotted in Fig. 2(c). Both increase almost linearly with the increasing layer numbers. The calculated polarization values for 2L–7L ReS_2 are ranging from 0.07 to 0.68 pC/m, which are comparable to that in the experimentally reported value for $1\text{T}'\text{-WTe}_2$ at around 0.28 pC/m [31].

Synthesis and characterization of single-crystal $1\text{T}'\text{-ReS}_2$.— ReS_2 crystals [see the inset of Fig. 3(a)] were synthesized via the chemical vapor transport (CVT) method [51,52] with appropriate improvement (see details in the Supplemental Material, S2 [50]). X-ray diffraction (XRD) patterns indicate that the synthesized ReS_2 samples are crystallized in triclinic structure [Fig. 3(b)]. The narrow full width at half maximum of the XRD peak [the inset of Fig. 3(b)] indicates the superior crystallization quality of the as-synthesized ReS_2 . To further evaluate the crystallographic structure, we transferred ReS_2 nanoflakes onto a

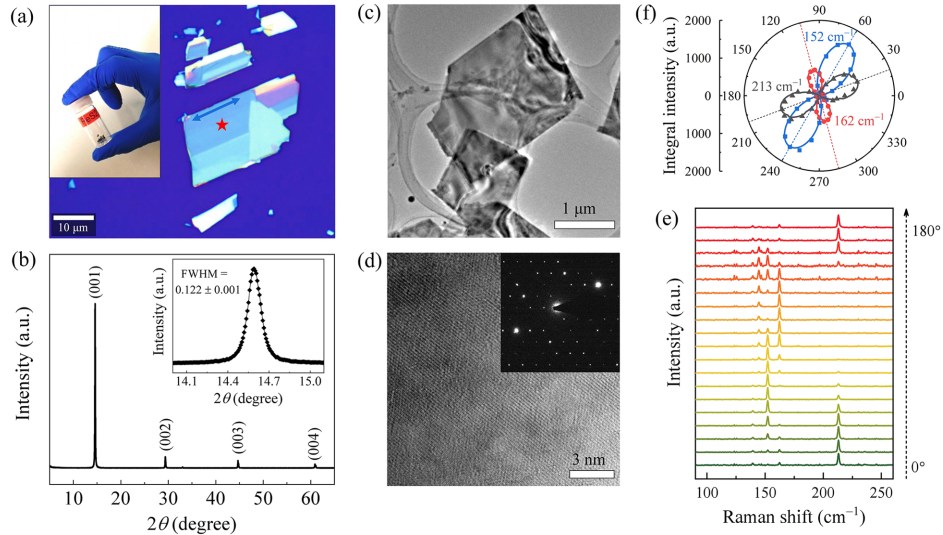


FIG. 3. (a) Optical image of ReS_2 mechanically transferred onto Si/SiO_2 . Inset: the synthesized ReS_2 bulks. (b) XRD pattern of ReS_2 bulk crystals. (c),(d) TEM images of ReS_2 . Inset in (d): corresponding SAED pattern, showing only one set of diffraction spots. (e) Excitation angle dependence of the Raman spectra for ReS_2 . (f) Polar plots of three representative Raman features. The dashed lines indicate the orientation of the principal axis for each mode.

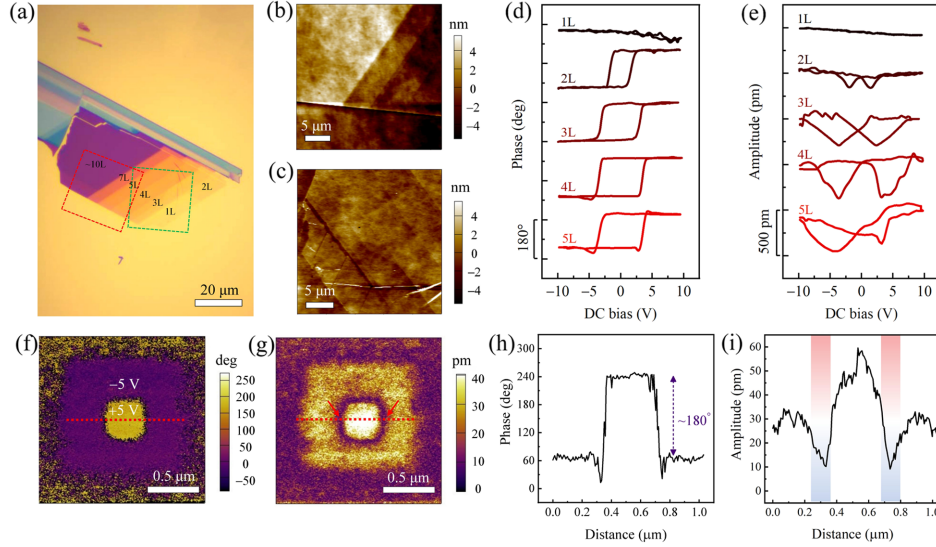


FIG. 4. (a) Optical image of a ReS_2 flake transferred onto Au-coated quartz substrate. The sample surface is atomically flat with occasional terraces from the cleaving process. (b),(c) AFM images corresponding to the region marked by red and green dashed squares shown in (a), respectively. (d),(e) PFM phase hysteresis (d) and butterfly-shaped PFM amplitude-voltage loops (e) for 1L–5L ReS_2 . (f), (g) PFM phase (f) and amplitude (g) images for 4L ReS_2 on graphene, with a written box-in-box pattern acquired by opposite dc bias. (h),(i) Cross-sectional profiles of the PFM phase (h) and amplitude (i) signals along the red dotted lines as shown in (f) and (g).

copper microgrid [Fig. 3(c)] for high-resolution transmission electron microscopy (HRTEM) characterization. The HRTEM image (see details in the Supplemental Material, S3 [50]) clearly displays that the Re atoms dimerize to form the diamond-shaped chains along the crystallographic in-plane b axis, showing that the ReS_2 sample crystallizes in a thermally stable $1\text{T}'$ structure [Fig. 3(d)]. Furthermore, the selected area electron diffraction (SAED) pattern [inset, Fig. 3(d)] exhibits only one set of diffraction spots, confirming the single-crystalline nature.

With the synthesized $1\text{T}'$ - ReS_2 single crystal, we subsequently examined its characteristic structure anisotropy with Raman spectra. As shown in Fig. 3(e), the excitation angle-resolved Raman spectra were collected from a $1\text{T}'$ - ReS_2 sample as marked by a red pentagram in Fig. 3(a). The intensity of each Raman peak varies remarkably with the excitation angle, confirming the anisotropy of the synthesized ReS_2 sample. Specific peaks belonging to the A_g modes were observed at 152, 162, and 213 cm^{-1} [Fig. 3(f)], which can be attributed to the lattice vibrations associated with the motion of Re atoms (see the Supplemental Material, S4 [50]). Besides, there exists an approximate correspondence between the principal axis of the 213 cm^{-1} mode and the direction of b axis as marked by a blue double-headed arrow in Fig. 3(a). This correspondence further indicates the superior quality of $1\text{T}'$ - ReS_2 .

Experimental characterization of the ferroelectric properties.—The predicted ferroelectricity in $1\text{T}'$ - ReS_2 was investigated with the PFM technique. In consideration of the atomic thickness of 1L–10L $1\text{T}'$ - ReS_2 [Figs. 4(a)–4(c)], we used the ultrasmooth metal surfaces as substrates (Supplemental Material, S5 [50]) in the PFM measurements.

The transfer process for $1\text{T}'$ - ReS_2 multilayers is provided in the Supplemental Material, S6 [50]. For 2L–5L $1\text{T}'$ - ReS_2 , the PFM phase responses exhibit a single hysteresis loop with a phase contrast of $\sim 180^\circ$ [Fig. 4(d)], while the amplitude responses display a butterfly-shaped curve [Fig. 4(e)]. Besides, with the increasing layer number, we observed both the stronger PFM amplitude and the larger coercive voltage. These trends are in good consistency with our theoretical calculations. As a contrast, for 1L $1\text{T}'$ - ReS_2 , no such kind of ferroelectric switching behavior was observed. It verifies that ferroelectricity cannot exist in $1\text{T}'$ - ReS_2 monolayers since the inversion symmetry prohibits the emergence of polarization. In addition, due to the interface electrostatic or ion movement effects, previous studies have shown that ferroelectriclike PFM loops could also be obtained in some nonferroelectric materials [53,61]. To exclude these artifacts in our study, we replaced the Au-coated quartz substrates with graphene in subsequent PFM measurements. The graphene substrates enable a better ground connection and the applying of a homogeneous electric field (Supplemental Material, S7 [50]). In the $1\text{T}'$ - ReS_2 on graphene sample, we observed the same butterfly-shaped and single ferroelectric hysteresis loop in the PFM amplitude and phase spectra, which further consolidates our observations.

Another feature for ferroelectrics is the controllable domain engineering. To check this, we performed the electrical “read-and-write” operations in $1\text{T}'$ - ReS_2 on graphene [Figs. 4(f)–4(i)]. Figures 4(f) and 4(g) exhibit the PFM phase and amplitude images obtained from 4L $1\text{T}'$ - ReS_2 on graphene after writing a box-in-box pattern with opposite dc bias ($\pm 5\text{ V}$). The reversed oriented

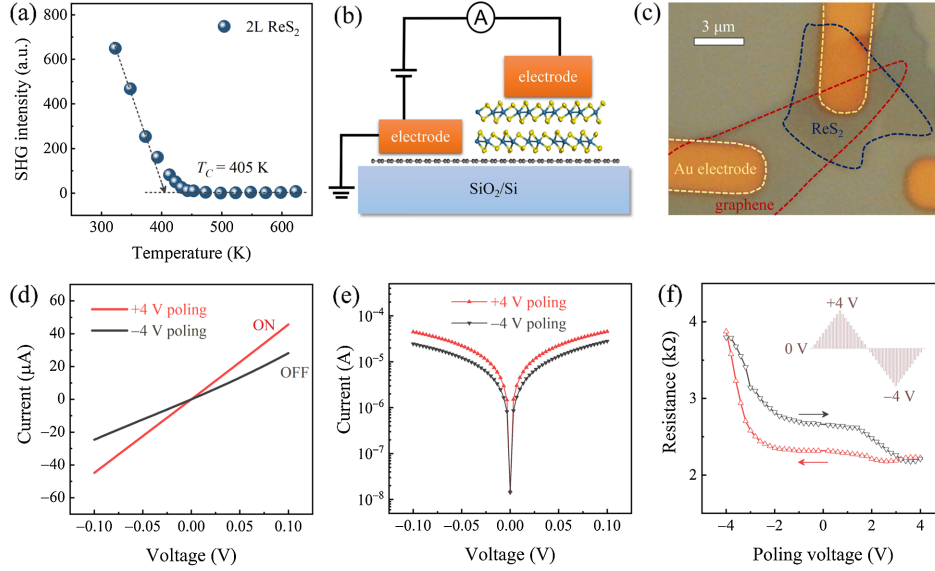


FIG. 5. (a) Temperature dependence of the SHG intensity of 2L ReS₂. (b) Schematic illustration of an FTJ based on 2L ReS₂ and 1L graphene. (c) Optical image of the ReS₂-based FTJ. (d),(e) I - V characteristics of the FTJ device, exhibiting tunneling electroresistance between the ON and OFF states, set by ± 4 V poling voltage. (f) Resistance as a function of the poling voltage with reading pulses of 0.1 V, measured by applying the voltage pulse train. Inset: the voltage pulse train, composed of writing pulses following a triangular profile between ± 4 V.

polarizations are clearly visualized in the PFM images, corresponding to the opposite external switching electric fields. From the PFM phase line profile [Fig. 4(h)], the phase inverts by $\sim 180^\circ$ between two adjacent domains, which indicates their antiparallel alignment states in the out-of-plane direction. Importantly, we observed clear dark lines in the PFM amplitude image as marked by red arrows in Fig. 4(g). This observation evidences the formation of domain walls between two adjacent artificial domains, because the domain walls are believed to be with vanished piezoresponse [see the enlarged line profile in Fig. 4(i)] due to the structural reconfiguration at domain boundaries. Furthermore, we find that the artificial domain patterns are identifiable after several hours of exposure under ambient conditions (Supplemental Material, S7-S9 [50]), which suggests the excellent ferroelectric stability in 1T'-ReS₂ multilayers.

Potential device application of ferroelectric 1T'-ReS₂.—2D ferroelectricity offers a platform for developing high-density memories and efficient information processing devices with low-energy consumption [54]. Before shedding light on the device application potential, there is need to examine the thermal stability of the vertical ferroelectricity in 1T'-ReS₂, which is of great importance to evaluate the functionality of ferroelectrics. Here, we measured the ferroelectric transition temperature (T_C) of 2L 1T'-ReS₂ by the temperature-dependent SHG measurements (Supplemental Material, S10, S11 [50]) [55]. As shown in Fig. 5(a), distinct SHG signals of 2L 1T'-ReS₂ are observed at room temperature, while the SHG intensity decreases gradually with the increasing temperature and

almost vanishes at temperatures above 450 K. Based on a simple fitting, we estimate the T_C of 2L 1T'-ReS₂ to be ~ 405 K. The high T_C endows semiconducting 1T'-ReS₂ a promising candidate for the field of sliding ferroelectricity towards realistic applications.

We then fabricated a prototype of the FTJ device using 2L ReS₂ as the tunneling layer and Au/graphene as the top and bottom contact electrodes as shown in Figs. 5(b) and 5(c). The electrical characteristics of the Au/1T'-ReS₂/graphene-based vdW FTJ are exhibited in Figs. 5(d)–5(f). The ON and OFF states can be switched by applying the poling voltages of ± 4 V, as shown in the I - V characteristics measurements in Figs. 5(d) and 5(e). The tunneling current under -0.1 V bias is lower ($|I_{\text{OFF}}| \sim 24.6 \mu\text{A}$) in the OFF state and higher ($|I_{\text{ON}}| \sim 44.8 \mu\text{A}$) in the ON state. Therefore, the FTJ device is with the tunneling electroresistance of around 1.82. As shown in Fig. 5(f), the tunneling resistance is plotted as a function of the poling voltage. Along with the sequence of applied poling voltage pulses, the resistance hysteresis loop follows the clockwise direction. Meanwhile, the switching voltages are consistent with the coercive field from the PFM results for 2L 1T'-ReS₂. The switching phenomenon in the FTJ device can be understood by Fermi level modulation in graphene, which is realized by ferroelectric polarization reversal [54]. The electrical characteristics of the vdW FTJ demonstrate the potentials of 1T'-ReS₂ for functional applications, which also confirms the nonvolatility of the explored 2D ferroelectricity.

Conclusion.—In summary, based on the combined study of theory and experiment, we have unambiguously demonstrated that 2D vertical ferroelectricity can be stabilized

in 1T'-ReS₂ multilayers, but is not existent in its centrosymmetric monolayers. Our results show that the robust ferroelectricity of 1T'-ReS₂ originates from interlayer charge transfer that depends on the in-plane slipping in the bilayer and multilayer forms. Thus, the emergence of ferroelectricity in 1T'-ReS₂ multilayers highlights the importance of interlayer engineering and provides a new possibility to manipulate the quantum states in vdW materials.

This work was supported by the National Key Research and Development Program of China (No. 2017YFA0205004), National Natural Science Foundation of China (No. 12004182, No. T2125004, No. 11774173, No. 61874003, No. 11674295, No. 51790492, and No. 51731001), Jiangsu Province Science Foundation (No. BK20200481), Anhui Initiative in Quantum Information Technologies (No. AHY170000), the Fundamental Research Funds for the Central Universities (No. 30920041115, No. 30920021148, No. 30920021152, No. WK3510000013, and No. WK2030020032), and Postdoctoral Science Foundation of China (No. 2021M691587). The authors thank Dr. Yu Ye from Peking University and Professor Zhenyu Zhang from University of Science and Technology of China for helpful discussions.

*Corresponding author.
lundai@pku.edu.cn

†Corresponding author.
hlzeng@ustc.edu.cn

‡Corresponding author.
ekan@njust.edu.cn

§These authors contributed equally to this work.

- [1] T. Hu and E. Kan, *Wiley Interdiscip. Rev. Comput. Mol. Sci.* **9**, e1409 (2019).
- [2] J. Shang, X. Tang, and L. Kou, *Wiley Interdiscip. Rev. Comput. Mol. Sci.* **11**, e1496 (2021).
- [3] E. Kan, F. Wu, K. Deng, and W. Tang, *Appl. Phys. Lett.* **103**, 193103 (2013).
- [4] M. Wu and X. C. Zeng, *Nano Lett.* **16**, 3236 (2016).
- [5] T. Hu, H. Wu, H. Zeng, K. Deng, and E. Kan, *Nano Lett.* **16**, 8015 (2016).
- [6] W. Ding, J. Zhu, Z. Wang, Y. Gao, D. Xiao, Y. Gu, Z. Zhang, and W. Zhu, *Nat. Commun.* **8**, 14956 (2017).
- [7] M. Wu and X. C. Zeng, *Nano Lett.* **17**, 6309 (2017).
- [8] C. Huang, Y. Du, H. Wu, H. Xiang, K. Deng, and E. Kan, *Phys. Rev. Lett.* **120**, 147601 (2018).
- [9] L. Ma, Y. Jia, S. Ducharme, J. Wang, and X. C. Zeng, *J. Am. Chem. Soc.* **141**, 1452 (2019).
- [10] M. Xu, C. Huang, Y. Li, S. Liu, X. Zhong, P. Jena, E. Kan, and Y. Wang, *Phys. Rev. Lett.* **124**, 067602 (2020).
- [11] J. Zhang, X. Shen, Y. Wang, C. Ji, Y. Zhou, J. Wang, F. Huang, and X. Lu, *Phys. Rev. Lett.* **125**, 017601 (2020).
- [12] K. Chang, J. Liu, H. Lin, N. Wang, K. Zhao, A. Zhang, F. Jin, Y. Zhong, X. Hu, and W. Duan, *Science* **353**, 274 (2016).
- [13] N. Higashitarumizu, H. Kawamoto, C.-J. Lee, B.-H. Lin, F.-H. Chu, I. Yonemori, T. Nishimura, K. Wakabayashi, W.-H. Chang, and K. Nagashio, *Nat. Commun.* **11**, 2428 (2020).
- [14] T. Ghosh, M. Samanta, A. Vasdev, K. Dolui, J. Ghatak, T. Das, G. Sheet, and K. Biswas, *Nano Lett.* **19**, 5703 (2019).
- [15] A. Belianinov, Q. He, A. Dziazgys, P. Maksymovych, E. Eliseev, A. Borisevich, A. Morozovska, J. Banys, Y. Vysochanskii, and S. V. Kalinin, *Nano Lett.* **15**, 3808 (2015).
- [16] F. Liu, L. You, K. L. Seyler, X. Li, P. Yu, J. Lin, X. Wang, J. Zhou, H. Wang, and H. He, *Nat. Commun.* **7**, 12357 (2016).
- [17] L. You, Y. Zhang, S. Zhou, A. Chaturvedi, S. A. Morris, F. Liu, L. Chang, D. Ichinose, H. Funakubo, and W. Hu, *Sci. Adv.* **5**, eaav3780 (2019).
- [18] J. A. Brehm, S. M. Neumayer, L. Tao, A. O'Hara, M. Chyasnavichus, M. A. Susner, M. A. McGuire, S. V. Kalinin, S. Jesse, and P. Ganesh, *Nat. Mater.* **19**, 43 (2020).
- [19] D.-D. Xu, R.-R. Ma, A.-P. Fu, Z. Guan, N. Zhong, H. Peng, P.-H. Xiang, and C.-G. Duan, *Nat. Commun.* **12**, 655 (2021).
- [20] X. Wang, C. Zhu, Y. Deng, R. Duan, J. Chen, Q. Zeng, J. Zhou, Q. Fu, L. You, S. Liu, J. H. Edgar, P. Yu, and Z. Liu, *Nat. Commun.* **12**, 1109 (2021).
- [21] Y. Li, J. Fu, X. Mao, C. Chen, H. Liu, M. Gong, and H. Zeng, *Nat. Commun.* **12**, 5896 (2021).
- [22] S. Yuan, X. Luo, H. L. Chan, C. Xiao, Y. Dai, M. Xie, and J. Hao, *Nat. Commun.* **10**, 1 (2019).
- [23] Y. Zhou, D. Wu, Y. Zhu, Y. Cho, Q. He, X. Yang, K. Herrera, Z. Chu, Y. Han, M. C. Downer, H. Peng, and K. Lai, *Nano Lett.* **17**, 5508 (2017).
- [24] C. Cui, W.-J. Hu, X. Yan, C. Addiego, W. Gao, Y. Wang, Z. Wang, L. Li, Y. Cheng, P. Li, X. Zhang, H. N. Alshareef, T. Wu, W. Zhu, X. Pan, and L.-J. Li, *Nano Lett.* **18**, 1253 (2018).
- [25] S. Wan, Y. Li, W. Li, X. Mao, W. Zhu, and H. Zeng, *Nanoscale* **10**, 14885 (2018).
- [26] S. Wan, Y. Li, W. Li, X. Mao, C. Wang, C. Chen, J. Dong, A. Nie, J. Xiang, and Z. Liu, *Adv. Funct. Mater.* **29**, 1808606 (2019).
- [27] M. Si, A. K. Saha, S. Gao, G. Qiu, J. Qin, Y. Duan, J. Jian, C. Niu, H. Wang, W. Wu, S. K. Gupta, and P. D. Ye, *Nat. Electron.* **2**, 580 (2019).
- [28] Y. Li, C. Chen, W. Li, X. Mao, H. Liu, J. Xiang, A. Nie, Z. Liu, W. Zhu, and H. Zeng, *Adv. Electron. Mater.* **6**, 2000061 (2020).
- [29] A. Weston, Y. Zou, V. Enaldiev, A. Summerfield, N. Clark, V. Zolyomi, A. Graham, C. Yelgel, S. Magorrian, M. Zhou, J. Zultak, D. Hopkinson, A. Barinov, T. H. Bointon, A. Kretinin, N. R. Wilson, P. H. Beton, V. I. Fal'ko, S. J. Haigh, and R. Gorbachev, *Nat. Nanotechnol.* **15**, 592 (2020).
- [30] L. Li and M. Wu, *ACS Nano* **11**, 6382 (2017).
- [31] Z. Fei, W. Zhao, T. A. Palomaki, B. Sun, M. K. Miller, Z. Zhao, J. Yan, X. Xu, and D. H. Cobden, *Nature (London)* **560**, 336 (2018).
- [32] Q. Yang, M. Wu, and J. Li, *J. Phys. Chem. Lett.* **9**, 7160 (2018).
- [33] P. Sharma, F.-X. Xiang, D.-F. Shao, D. Zhang, E. Y. Tsymlal, A. R. Hamilton, and J. Seidel, *Sci. Adv.* **5**, eaax5080 (2019).

- [34] Z. Zheng, Q. Ma, Z. Bi, S. de la Barrera, M.-H. Liu, N. Mao, Y. Zhang, N. Kiper, K. Watanabe, T. Taniguchi, J. Kong, W. A. Tisdale, R. Ashoori, N. Gedik, L. Fu, S.-Y. Xu, and P. Jarillo-Herrero, *Nature (London)* **588**, 71 (2020).
- [35] K. Yasuda, X. Wang, K. Watanabe, T. Taniguchi, and P. Jarillo-Herrero, *Science* **372**, 1458 (2021).
- [36] M. V. Stern, Y. Waschitz, W. Cao, I. Nevo, K. Watanabe, T. Taniguchi, E. Sela, M. Urbakh, O. Hod, and M. B. Shalom, *Science* **372**, 1462 (2021).
- [37] Y. Cao, V. Fatemi, S. Fang, K. Watanabe, T. Taniguchi, E. Kaxiras, and P. Jarillo-Herrero, *Nature (London)* **556**, 43 (2018).
- [38] Y. Cao, V. Fatemi, A. Demir, S. Fang, S. L. Tomarken, J. Y. Luo, J. D. Sanchez-Yamagishi, K. Watanabe, T. Taniguchi, E. Kaxiras, R. C. Ashoori, and P. Jarillo-Herrero, *Nature (London)* **556**, 80 (2018).
- [39] T. M. R. Wolf, J. L. Lado, G. Blatter, and O. Zilberberg, *Phys. Rev. Lett.* **123**, 096802 (2019).
- [40] Z. Luo, M. Yang, Y. Liu, and M. Alexe, *Adv. Mater.* **33**, 2005620 (2021).
- [41] D. A. Chenet, O. B. Aslan, P. Y. Huang, C. Fan, A. M. Van Der Zande, T. F. Heinz, and J. C. Hone, *Nano Lett.* **15**, 5667 (2015).
- [42] E. Zhang, Y. Jin, X. Yuan, W. Wang, C. Zhang, L. Tang, S. Liu, P. Zhou, W. Hu, and F. Xiu, *Adv. Funct. Mater.* **25**, 4076 (2015).
- [43] M. Rahman, K. Davey, and S.-Z. Qiao, *Adv. Funct. Mater.* **27**, 1606129 (2017).
- [44] A. Dhara, D. Chakrabarty, P. Das, A. K. Pattanayak, S. Paul, S. Mukherjee, and S. Dhara, *Phys. Rev. B* **102**, 161404(R) (2020).
- [45] D. Li, S. Sun, Z. Xiao, J. Song, D.-F. Shao, E. Y. Tsymbal, S. Ducharme, and X. Hong, *Phys. Rev. Lett.* **127**, 136803 (2021).
- [46] G. Kresse and J. Hafner, *Phys. Rev. B* **48**, 13115 (1993).
- [47] G. Kresse and J. Furthmüller, *Comput. Mater. Sci.* **6**, 15 (1996).
- [48] G. Kresse and D. Joubert, *Phys. Rev. B* **59**, 1758 (1999).
- [49] J. P. Perdew, K. Burke, and M. Ernzerhof, *Phys. Rev. Lett.* **77**, 3865 (1996).
- [50] See Supplemental Material at <http://link.aps.org/supplemental/10.1103/PhysRevLett.128.067601> for methods, two energy-degenerate ferroelectric structures of 2L ReS₂, the CVT process, HRTEM images, Raman modes fitting, ultrasmooth metal surfaces, transfer process, switchable polarization in ReS₂ on graphene, ferroelectric domain distributions, the experimental setup for SHG, and SHG for 1L and 2L ReS₂, which includes Refs. [51–60].
- [51] Z. Lai, A. Chaturvedi, Y. Wang, T. H. Tran, X. Liu, C. Tan, Z. Luo, B. Chen, Y. Huang, and G.-H. Nam, *J. Am. Chem. Soc.* **140**, 8563 (2018).
- [52] C. Liang, Y. Chan, K. Tiong, Y. Huang, Y. Chen, D. Dumcenco, and C. Ho, *J. Alloys Compd.* **480**, 94 (2009).
- [53] A. Gruverman, M. Alexe, and D. Meier, *Nat. Commun.* **10**, 1661 (2019).
- [54] J. Wu, H.-Y. Chen, N. Yang, J. Cao, X. Yan, F. Liu, Q. Sun, X. Ling, J. Guo, and H. Wang, *Nat. Electron.* **3**, 466 (2020).
- [55] Y. Song, S. Hu, M.-L. Lin, X. Gan, P.-H. Tan, and J. Zhao, *ACS Photonics* **5**, 3485 (2018).
- [56] L. Hart, S. Dale, S. Hoye, J. L. Webb, and D. Wolverson, *Nano Lett.* **16**, 1381 (2016).
- [57] S. Zhang, N. Mao, N. Zhang, J. Wu, L. Tong, and J. Zhang, *ACS Nano* **11**, 10366 (2017).
- [58] P. Nagpal, N. C. Lindquist, S.-H. Oh, and D. J. Norris, *Science* **325**, 594 (2009).
- [59] K. S. Novoselov, A. K. Geim, S. V. Morozov, D. Jiang, S. V. Dubonos, I. V. Grigorieva, and A. A. Firsov, *Science* **306**, 666 (2004).
- [60] A. Castellanos-Gomez, M. Buscema, R. Molenaar, V. Singh, L. Janssen, H. S. J. van der Zant, and G. A. Steele, *2D Mater.* **1**, 011002 (2014).
- [61] L. Collins, Y. Liu, O. S. Ovchinnikova, and R. Proksch, *ACS Nano* **13**, 8055 (2019).